Computational Materials Science 201 (2022) 110887

Contents lists available at ScienceDirect

Computational Materials Science

journal homepage: www.elsevier.com/locate/commatsci

On the formation of {11$\bar{2}$2} boundary via {10$\bar{1}$2}-{01$\bar{1}$2} twin–twin interaction in magnesium

Amir Hassan Zahiri[1], Luiz Carneiro[1], Jamie Ombogo, Pranay Chakraborty, Lei Cao *

Department of Mechanical Engineering, University of Nevada, Reno, Reno, NV, 89557, USA

ARTICLE INFO

Keywords:
Twinning
Magnesium
Strain hardening

ABSTRACT

{10$\bar{1}$2} twinning occurs extensively in Mg to accommodate plastic deformation. With multiple active twin variants, twin–twin interaction occurs and this often forms twin–twin boundaries. In this work, the {11$\bar{2}$2} twin–twin boundary is studied using electron backscatter diffraction (EBSD) analysis and atomistic simulations. EBSD data show that many of the twin–twin boundaries align well with {11$\bar{2}$2} or {11$\bar{2}$6} planes. Further, atomistic simulations reveal dynamically the formation of {11$\bar{2}$2} boundary via the interaction of two non-co-zone {10$\bar{1}$2} twin variants. Moreover, the twinning mode of the {11$\bar{2}$2} boundary is found to be an extension twin with second undistorted plane of {11$\bar{2}$6}. In addition, the {11$\bar{2}$2} boundaries contribute significantly to the 60° ⟨01$\bar{1}$0⟩ peak in the misorientation histogram; they also play an essential role in the unique strong strain hardening under *c*-axis tension. Our findings are crucial for completing the twinning theories for Mg.

1. Introduction

Deformation twinning in Mg has been explored in great details over the past decades because of its profuse quantity even at room temperature and its significance to the strength and strain hardenings [1–12]. The operative twinning modes in Mg include {10$\bar{1}$2} extension twin, {10$\bar{1}$1} contraction twin, and {10$\bar{1}$1}-{10$\bar{1}$2}/{10$\bar{1}$3}-{10$\bar{1}$2} double twins [13,14]. Due to its relatively low activation stress, the {10$\bar{1}$2} twin is the predominant twinning mode and often constitutes the majority of twins characterized experimentally. When one particular {10$\bar{1}$2} twin variant has the highest Schmid factor, a large number of grains are found to twin on this variant. On the other hand, when multiple {10$\bar{1}$2} variants have similarly high Schmid factors, many grains are found to twin simultaneously on different {10$\bar{1}$2} variants [15]. When different {10$\bar{1}$2} variants within the same grain grow into each other, their interactions lead to the formation of complex twin–twin structures and twin–twin boundaries [16–19].

Early studies on twin–twin interactions in hcp metals revealed the strong correlation between twin–twin interactions and strain hardening [20–22]. In addition, a study of tension–compression of single crystal Mg reported that twin–twin boundaries are critical to the retardation of detwinning, because of the unfavorable dissociation of twin–twin boundary dislocations [23]. In the electron backscatter diffraction (EBSD) misorientation histogram of pure Mg and it alloys [16,24], the prominent peak at 87° with a ⟨$\bar{1}$2$\bar{1}$0⟩ rotation axis corresponds to the {10$\bar{1}$2} twins. Additionally, another peak is often observed at 55-60° with a ⟨01$\bar{1}$0⟩ rotation axis and is attributed to twin–twin boundaries [16–18]. This local misorientation peak suggests that the twin–twin boundaries exist in large quantities, which has stimulated further studies on twin–twin boundaries.

Yu et al. [18] conducted a systematic study on the twin–twin interactions in Mg using EBSD and theoretical analysis. They found several possible twin–twin boundary planes, which is determined by the crystallographical orientation of the interacting primary {10$\bar{1}$2} twins. Among the twin–twin interactions reported, the case of {11$\bar{2}$2} boundary is particularly interesting because {11$\bar{2}$2} twin is one of the predominant twinning modes in other hcp metals, such as Ti and Zr [25–29]. In fact, there have been several preliminary evidences that {11$\bar{2}$2} twins might exist in hcp Mg, though a solid conclusion is still lacking. For example, {11$\bar{2}$2} and {11$\bar{2}$6} twins were observed in Ostapovets et al.'s experiment and molecular dynamics (MD) simulation, which was interpreted as the product of {10$\bar{1}$2}-{10$\bar{1}$2} double twins where the primary twin is completely retwinned into the secondary twin [30]. In addition, Cayron observed {11$\bar{2}$2} and {11$\bar{2}$6} twins in Mg single crystal experimentally [31] and proposed a one-step twinning mechanism based on a (58°, ⟨01$\bar{1}$0⟩) prototype stretch twin [32]. More recently, Chen et al. combined experiments and MD simulations to study twin–twin interactions and found that 60°⟨01$\bar{1}$0⟩ boundaries form through the impingement of different {10$\bar{1}$2} twin variants. They concluded that these boundaries are not {11$\bar{2}$2} twin

* Corresponding author.
E-mail address: leicao@unr.edu (L. Cao).
[1] These two authors contributed equally.

https://doi.org/10.1016/j.commatsci.2021.110887
Received 9 July 2021; Received in revised form 31 August 2021; Accepted 14 September 2021
Available online 30 September 2021

boundaries, because these boundaries do not align with any $\{11\bar{2}2\}$ planes and are rather incoherent [33].

Though there were a few reports of $\{11\bar{2}2\}$ twins in Mg, neither the post-mortem experimental characterization [18,30,31] nor the theoretical proposal of a new twinning mode [32,34] can reveal the dynamic formation process. Without capturing the dynamic process, the same post-mortem experimental characterization—$\{11\bar{2}2\}$ boundary in Mg—could be attributed to fundamentally different mechanisms following different formation pathways [30,32–34]. Moreover, its relevance to $\{11\bar{2}2\}$ twins remain largely unknown. In this work, we aim to gain an in-depth understanding of the twin–twin interactions and possible formation of $\{11\bar{2}2\}$ boundaries in Mg through combined experimental characterization and atomistic modeling. Specifically, the crystallographic planes of the twin–twin boundaries are characterized experimentally using EBSD analysis, and the dynamic formation process of the twin–twin boundary and the equivalent twinning mode are analyzed using atomistic simulations. In addition, its possible contribution to the EBSD misorientation peak of 55-60° $\langle 01\bar{1}0\rangle$ and to the strong strain hardening present in the stress–strain curves are also discussed. The findings in this work will be an important step for completing the twin formation theories in Mg and bridging theories with experimental observations.

This paper is organized as follows. In Section 2 we describe the methods for experiments and atomistic simulations. In Section 3 we present the results and study and analyze our finding obtained from experiments and simulations. In Section 4 we discuss the effect of twin–twin boundaries on misorientation peak and strain hardening rate in more details. Finally, we present the conclusions in Section 5.

2. Material and methods

2.1. Experiments

The sample used for the mechanical experiments is a 76.2-mm-thick rolled AZ31B (Mg-3Al-1Zn) plate. The EBSD scan is taken on three orthotropic planes: normal direction, rolling direction, and transverse direction. The initial microstructure consists of nearly equiaxial grains with an average grain size of approximately 50 μm. Due to rolling, the sample presents a strong basal texture with the c-axes of most grains oriented approximately parallel to the normal direction.

During the mechanical loading, the rolled AZ31B is compressed along the rolling direction using a servo-hydraulic axial-torsion Instron fatigue testing machine with an axial load capacity of ±222 kN. The tests are conducted under strain control at a strain rate of 0.005 s^{-1}. The strain is measured using a clip-on extensometer with a gage length of 12.7 mm and a strain range of ±0.40. The specimens are machined along the rolling direction and have a solid cross-section with a 14 mm gage length and an 8 mm diameter.

The microstructure is characterized using companion specimens tested up to the strains of 0.01, 0.02, 0.04, 0.06, 0.08, and up to fracture (strain of 0.15). Cross-section samples for EBSD analysis are cut from the gage section of the tested specimen with the scan plane perpendicular to the loading direction. The samples are mechanically ground using SiC sandpapers down to P1200 grit size, followed by vibratory polishing using aluminum oxide with particle size of 0.05 μm and etching with 3% Nital for 5 s. The EBSD scans are taken in a Joel 7100 F field emission scanning electron microscope equipped with an Oxford HKL Channel 5 instrument at an acceleration voltage of 20 kV. The working distance is 25 mm, and the step size is 0.7 μm for the scanned area of 500×500 μm^2.

The EBSD scans are analyzed to construct the inverse pole figure and band contrast map. Following the label convention adopted by Yu et al. [18], the symbols T_i (i=1–6) represent the six $\{10\bar{1}2\}$ twin variants. T_1 represents the $(10\bar{1}2)[\bar{1}011]$ variant, while increasing subscripts correspond to other variants rotated counter-clockwise around the c-axis. The twin boundaries identified in the band contrast maps are $\{10\bar{1}2\}$ extension twin boundary (86° ± 5°$\langle 1\bar{2}10\rangle$), $\{10\bar{1}1\}$ compression twin boundary (56°±5°$\langle 1\bar{2}10\rangle$), and compression–extension double twin boundary (37.5°±5°$\langle 1\bar{2}10\rangle$). The twin–twin boundaries are identified as non-co-zone ones (60° ± 5°$\langle 10\bar{1}0\rangle$) and co-zone ones (7.4° ± 5°$\langle 1\bar{2}10\rangle$).

2.2. Molecular dynamics simulations

The molecular dynamics (MD) simulations are performed using the LAMMPS package [35]. The interactions between Mg atoms are modeled by the embedded-atom model potential developed by Wilson and Mendelev [36]. Periodic boundary conditions are applied in all three directions and the integration time step of 1 fs is used. Microstructure evolution is visualized using OVITO [37]. Common neighbor analysis [38,39] is adopted to identify the crystalline structure, with hcp, fcc, bcc, and non-crystalline atoms shown in cyan, green, red and yellow, respectively. Mechanical loading is applied at a constant strain rate of 10^8 s^{-1} and under a temperature of 10 K to reduce the effect of thermal fluctuation.

Initially, one million Mg atoms are created in a simulation box of $32 \times 28 \times 26$ nm^3. Then the temperature is increased gradually from 300 K to 1248 K, which is well above the melting point of Mg (923 K). In order to ensure that the Mg single crystal melts completely, the entire simulation domain is then relaxed using an isothermal–isobaric ensemble with the pressure set to 1 atm and the temperature to 1248 K for 500 ps. Subsequently, the Mg melt is quenched from 1248 K to room temperature with a cooling rate of 0.135 K/ps, which is then relaxed by two consecutive energy minimization to guarantee a complete relaxation of the internal force and stress. The quenching process leads to a nanotwinned Mg that further detwins under the loading of z-axis tension. Finally, we obtain a single crystal Mg with residual defects, such as basal stacking faults, I_1 stacking faults, pyramidal and prismatic dislocations. This single crystal Mg is referred to as the initial structure (parent phase) in the simulation section.

3. Results

3.1. Experiments

3.1.1. Twin structure evolution

When the AZ31B plate is subjected to compression along the rolling direction, $\{10\bar{1}2\}$ extension twins have a high Schmid factor and nucleate at early stages of deformation. As shown in Fig. 1, the microstructure is heavily twinned and the twin volume fraction reaches 68% at a strain of 6%. Besides considerable extension twin boundaries (the blue boundaries in the band contrast map), the activation of multiple twin variants in the same grain induces a substantial amount of twin–twin interactions, forming many twin–twin boundaries (the yellow and green boundaries in the band contrast map in Fig. 1a). For instance, grain G1, depicted in Fig. 1b, is heavily twinned by two non-co-zone $\{10\bar{1}2\}$ extension twin variants, T_4 and T_5. The analysis of the T_4–T_5 boundaries show that these boundaries lie almost parallel to the $\{11\bar{2}2\}$ or $\{11\bar{2}6\}$ plane traces of both T_4 and T_5, as marked in the band contrast map in Fig. 1b. The stereographic projections of the $\{11\bar{2}2\}$ and $\{11\bar{2}6\}$ plane zones of T_4 and T_5 are also presented in Fig. 1b. It is noted that T_4 and T_5 have intersecting $\{11\bar{2}2\}$ or $\{11\bar{2}6\}$ planes (dotted circles), indicating that $\{11\bar{2}2\}$ and $\{11\bar{2}6\}$ planes of each twin variant are parallel.

With further deformation, the majority of the grains are fully twinned and the total twin volume fraction reaches 98% before fracture (15% strain). As shown in Fig. 2, a large number of twin–twin boundaries are visible in grains with multiple active twin variants. For instance, grain G2, depicted in Fig. 2b, is fully twinned by T_3 and T_2 (or T_6 and T_5). As shown by the band contrast map of grain G2 in Fig. 2(b), the interaction of the non-co-zone twins completely eliminates the blue boundaries and only leaves the green boundaries, which align well with $\{11\bar{2}2\}$ or $\{11\bar{2}6\}$ planes. The stereographic projections of the $\{11\bar{2}2\}$

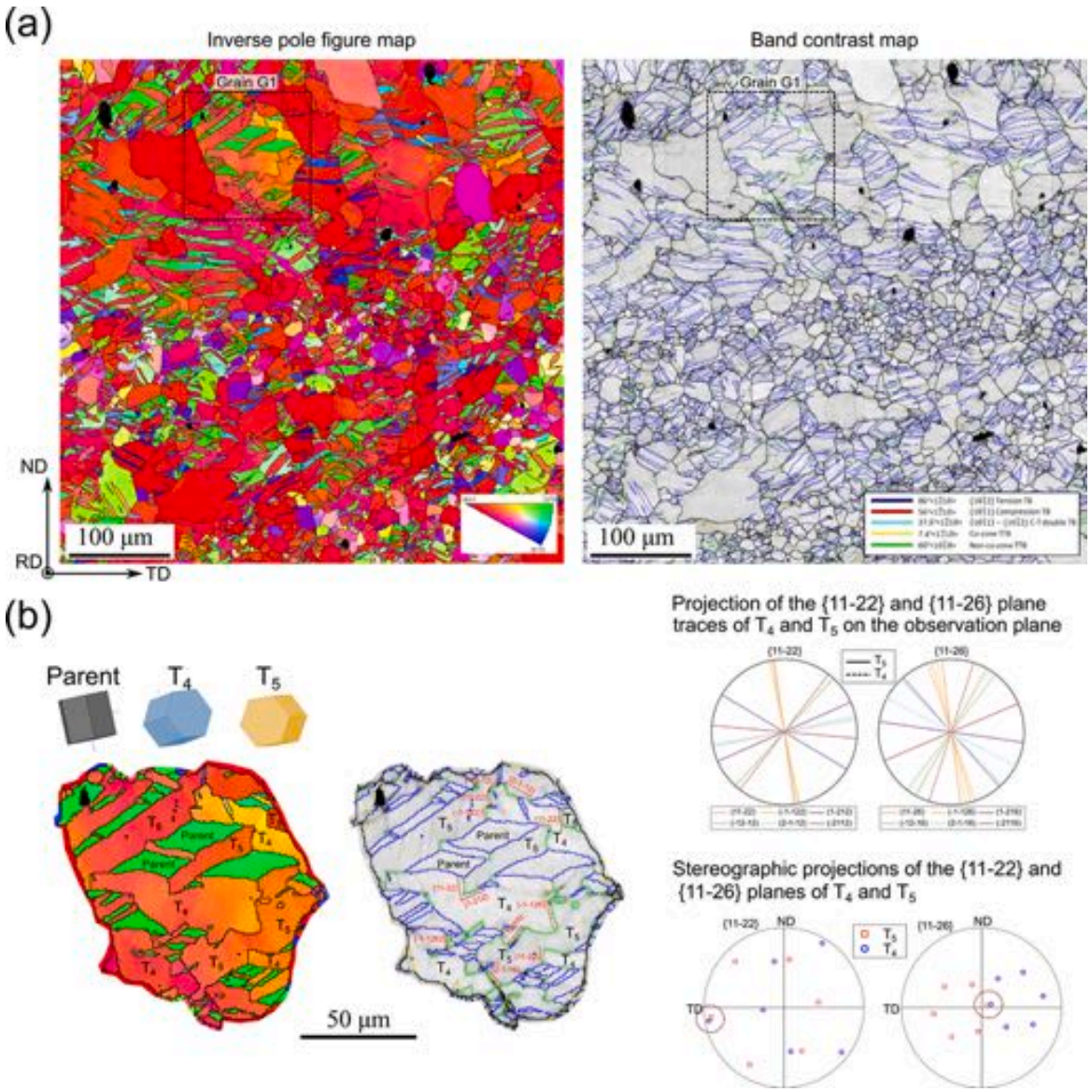

Fig. 1. EBSD inverse pole figure maps and band contrast maps of rolled AZ31B plate subjected to a compressive strain of 6%. (a) 500×500 μm^2 scan; (b) detailed representation of Grain G1 showing the $\{10\bar{1}2\}$ twin variants and trace analysis of twin–twin boundaries (green). The stereographic projections of the $\{11\bar{2}2\}$ and $\{11\bar{2}6\}$ planes of the twin variants are also represented.

and $\{11\bar{2}6\}$ plane zones show that T_3 and T_2 have intersecting planes (dotted circles), indicating that $\{11\bar{2}2\}$ and $\{11\bar{2}6\}$ planes of each twin variant are parallel. More detailed microstructure characterization at all strain levels tested can be found in Carneiro et al.'s work [19]. Notably, these $\{11\bar{2}2\}$ boundaries exhibit a twin-like morphology, as shown in the band contrast map in Fig. 2b. Thus, its relationship to the $\{11\bar{2}2\}$ twins will be investigated later in the simulation section.

3.1.2. Strain hardening rate

The evolution of the stress as well as the plastic strain hardening rate has been quantified in coauthor Carneiro's work on the twinning characteristics under three loading conditions [19]. As shown in Fig. 3a, the evolution of the plastic strain hardening rate shows three distinct stages: fast decrease due to microscopic yielding (Stage I), sequential increase (Stage II), and progressive decrease (Stage III) until fracture. In general, the strong strain hardening in Mg and its alloys is attributed to texture hardening and dynamic Hall–Petch effect [40,41], the latter of which is caused by the impedance of dislocations by primary $\{10\bar{1}2\}$ twin boundaries. Here, to understand the mechanism behind the monotonic increasing strain hardening in Stage II, the evolution of the length fraction of twin boundaries and twin–twin boundaries of different types is shown in Fig. 3b. Specifically, during Stage II, the fractions of the total twin boundaries as well as the $\{10\bar{1}2\}$ twin boundaries decrease, while the twin–twin boundary length fraction of both co–zone and non-co-zone types keeps increasing. This correlation between the increasing twin–twin boundary length fraction and the increasing strain hardening rate indicates that the twin–twin boundary contributes significantly to the strain hardening in Mg alloys. Given this importance, we will further investigate its detailed formation process, its twin-like morphology, and the preferential alignment along $\{11\bar{2}2\}$ and $\{11\bar{2}6\}$ planes, which will be achieved in the next section using atomistic simulations. It is worth noting that the reducing strain hardening rate in Stage III was attributed to the activation of non-basal slip in the twinned grains, as revealed by crystal plasticity modeling in Ref. [19].

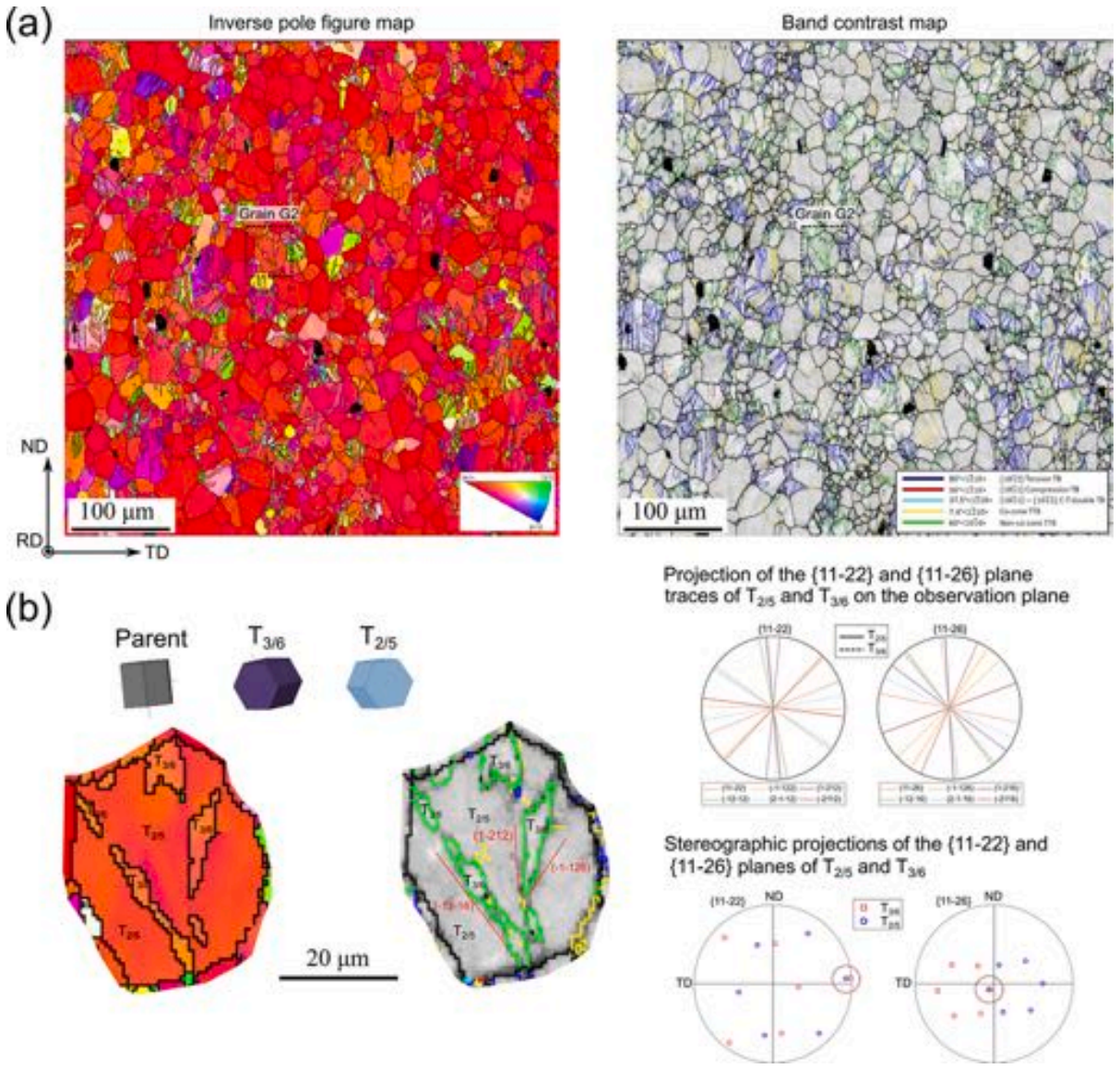

Fig. 2. EBSD inverse pole figure maps and band contrast maps of rolled AZ31B compressed to fracture, at a strain of 15%. (a) 500×500 μm^2 scan; (b) detailed representation of Grain G2 showing the $\{10\bar{1}2\}$ twin variants and trace analysis of twin–twin boundaries (green). The stereographic projections of the $\{11\bar{2}2\}$ and $\{11\bar{2}6\}$ planes of the twin variants are also represented.

3.2. Atomistic simulations

3.2.1. twin–twin interactions

To activate multiple twin variants, we apply tensile loading along the z-axis to the initial single crystal Mg constructed in Section 2.2. The first $\{10\bar{1}2\}$ twin variant (marked as T_2 in Fig. 4) nucleates at 0.88% strain. When the applied strain reaches 1.04%, the second $\{01\bar{1}2\}$ twin variant (marked as T_3) nucleates from a pyramidal dislocation that is pinned between two I_1 partial stacking faults (Fig. 4a). It should be noted that they are non-co-zone $\{10\bar{1}2\}$ variants as their common zone axes of twinning are different. The projection along the respective common zone axis of each extension twin is shown in Figs. 4c and 4d to demonstrate the twin relationship. Clearly, twin variant T_3 is misoriented by $86 \sim 89°$ around the $\langle 11\bar{2}0\rangle$ axis from the parent phase, which is the same for twin variant T_2 (Fig. 4c). With a high Schmid factor of 0.433, T_2 grows quickly upon strain increment and impinges on T_3 at a strain of 1.24% (Fig. 4b). In contrast, T_3 has a lower Schmid factor of 0.235 and grows at a much slower speed. With increasing strain, T_2 and T_3 grow into each other until, finally, the parent phase is completely consumed by T_2 at a strain of 12%.

Notably, the above process observed in our MD simulation follows the mechanism proposed by Nave and Barnett [16]. Specifically, based on experimental observation, they proposed that the parent structure twins on $\{10\bar{1}2\}$ and $\{01\bar{1}2\}$ planes simultaneously and the twin–twin boundary is formed around the less mobile twin variant when the parent is fully consumed by the more mobile twin variant. Indeed, the simultaneous twinning on two variants in our MD simulation results in the formation of $\{11\bar{2}2\}$ boundaries in between. Specifically, Fig. 5a shows the moment when T_2 and T_3 are about to meet each other, which is viewed from the c-axis of the parent structure. At this time, variants T_2 and T_3 are still bounded by $\{10\bar{1}2\}$ twin boundaries with respect to the parent structure. They then grow into each other and finally form a coherent boundary along the common $\{11\bar{2}2\}$ planes of T_2 and T_3 (Fig. 5b). Similar to our experimental observation in Fig. 2b, the newly formed boundary shows twin-like signatures, such as the lenticular morphology of T_3 shown in Fig. 5c. Furthermore, the misorientation between T_2 and T_3 is measured to be 62°, which is close to the theoretical misorientation angle of 63° for $\{11\bar{2}2\}$ twins [30]. Finally, the $\{11\bar{2}2\}$ boundaries consist of apparent three-atom unit

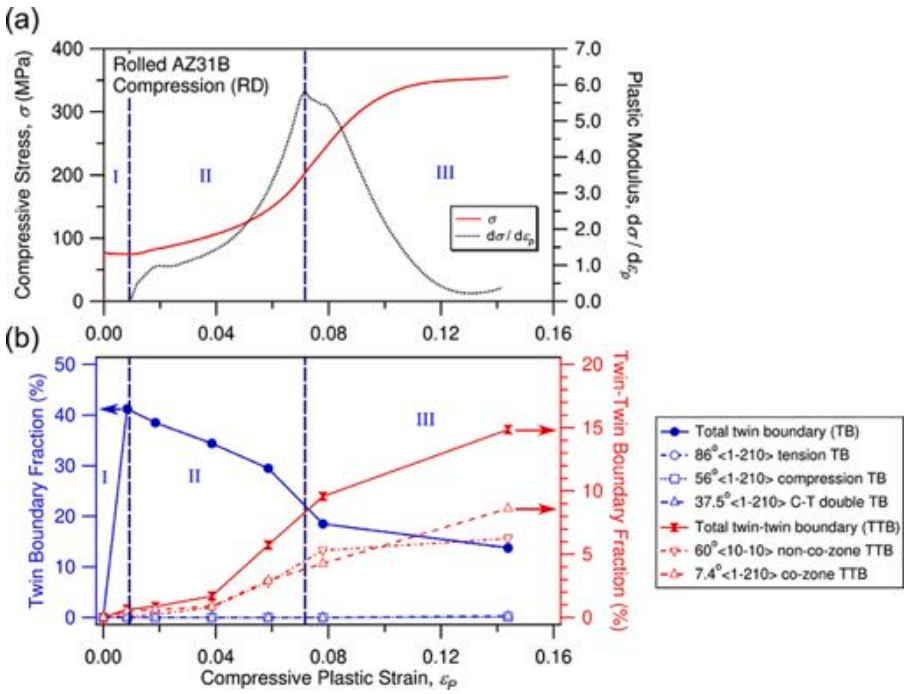

Fig. 3. Mechanical response and evolution of twin boundaries length fraction on rolled AZ31B plate compressed along the rolling direction until fracture. (a) Compressive stress–plastic strain (σ–ε_p) and plastic strain hardening rate ($d\sigma/d\varepsilon_p$–ε_p) curves; (b) twin–parent boundaries and twin–twin boundaries length fraction evolution.
Source: Adapted from Carneiro et al. [19]

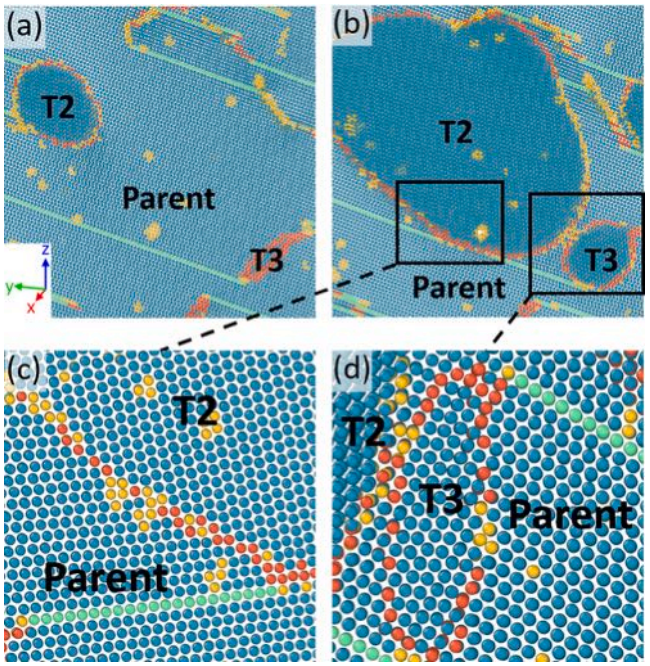

Fig. 4. Microstructure evolution in the Mg structure under the z-axis compression. (a) Nucleation of two twin variants T_2 and T_3 from the parent phase. (b) Fast growth of T_2 due to the high Schmid factor. (c) and (d) are the close-up views of the framed regions in (b) in the respect common zone axis, demonstrating the $\{10\bar{1}2\}$ extension twin relation.

structures (Fig. 5d) that has been identified as the atomistic signature of $\{11\bar{2}2\}$ twin boundary in previous MD simulations [42].

Previously, crystallographic analysis was conducted to understand the twin–twin interactions observed in Mg experiments [18,43]. Based on that a common interface bisecting two twinning planes, the twin–twin interaction boundary was predicted to be parallel to the $(1\bar{1}00)$ plane in the parent, which bonds $(\bar{1}2\bar{1}2)$ plane in one $\{10\bar{1}2\}$ twin and bonds $(\bar{2}11\bar{2})$ plane in the other $\{10\bar{1}2\}$ twin. In this work, our MD simulation demonstrates the dynamic process of the twin–twin interactions and provides direct evidence of the resulting formation of $\{11\bar{2}2\}$ twin-like boundaries. It should be noted that these boundaries can be coherent, as shown in Fig. 5d, in contrast to the incoherent boundaries observed in Chen et al.'s MD study [33].

3.2.2. Twinning mode

The equivalent twinning mode of the $\{11\bar{2}2\}$ twin–twin boundaries will be examined to understand its relevance to the previous reports of $\{11\bar{2}2\}$ twins in Mg and the $\{11\bar{2}2\}$ twins in Ti and Zr. To unambiguously distinguish the exact twinning mode, it is imperative to examine the second undistorted K_2 plane for the $\{11\bar{2}2\}$ twin-like boundaries in our MD simulation. To this end, we will follow the strategy of determining the K_2 plane for $\{10\bar{1}1\}$ transformation twins in Ti and Zr that are formed by quenching-induced bcc→hcp phase transformation [27]. Specifically, the assumption is that the two twin variants are crystallographically equivalent with respect to the parent structure. Therefore, the K_2/K_2' planes in the two daughter phases (T_2/T_3) should correspond to the same plane in the parent phase. As such, a $\{11\bar{2}0\}$ plane in the parent structure is traced during the deformation process, and is found to transform into $\{11\bar{2}6\}$ planes in both variants T_2 and T_3, as shown in Fig. 6. In other words, the twin–twin interaction induced $\{11\bar{2}2\}$ twin has a K_2 plane of $\{11\bar{2}6\}$ and its conjugate twinning mode is $\{11\bar{2}6\}$ twin.

Similar to the identification of the K_2 plane, the atoms near the $\{11\bar{2}2\}$ boundary are traced and the observed atomic movement is further plotted in the dichromatic complex in Fig. 7a. Obviously, this is a $q = 8$ mode and was referred to as b_4 $\{11\bar{2}2\}$ mode previously [44] (the subscript in b_4 represents the step height of the twinning disconnection). In principle, the $\{11\bar{2}2\}$ twinning mode observed in this work corresponds to the same twinning mode as in previous studies [30,32,34], though involving different formation mechanisms. Specifically, Ostapovets et al. [30] proposed a new twinning mode in

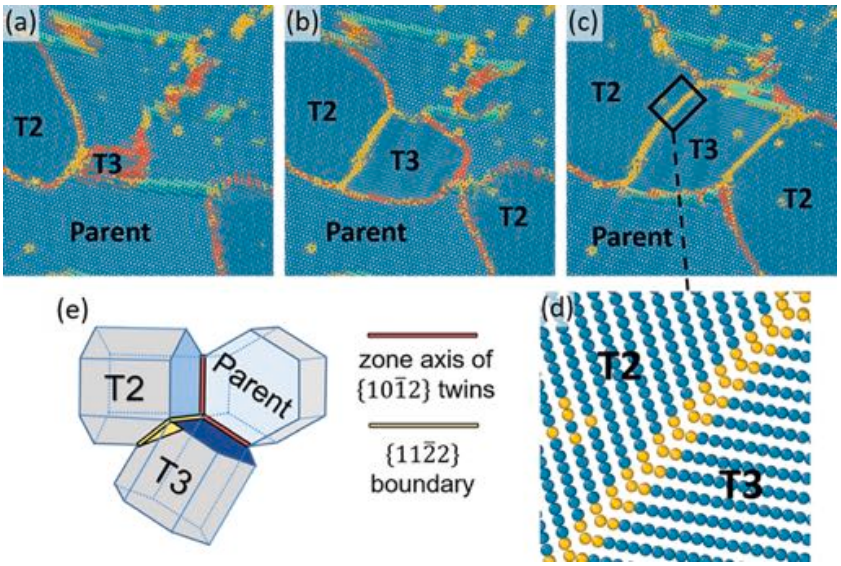

Fig. 5. The nucleation and growth of the two {10$\bar{1}$2} extension twins and the formation of coherent {11$\bar{2}$2} twin boundary. (a) The nucleation and (b) growth of T_2 and T_3, projected along the *c*-axis of the parent phase. (c) The interaction between T_2 and T_3 variants and formation of coherent {11$\bar{2}$2} twin boundary. (d) Formation of long coherent {11$\bar{2}$2} twin boundaries on both sides of variant T_3 due to the interaction with variant T2. (e) The orientation relation of the two {10$\bar{1}$2} variants and the parent phase.

Mg as {11$\bar{2}$2} extension twin, which is formed when the primary {10$\bar{1}$2} twin is completely re-twinned by a secondary {10$\bar{1}$2} twin. In addition, Cayron [32] proposed a new twinning mode of one-step ($58°, \boldsymbol{a}+\boldsymbol{2b}$) prototype stretch twin that has a habit plane of {11$\bar{2}$2} (or its conjugate {11$\bar{2}$6}). More recently, Gao et al. derived the {11$\bar{2}$2} extension twin using the well-known transformation matrices of hcp→bcc and bcc→hcp phase transformations [34].

Last but not the least, it is important to note that the {11$\bar{2}$2} here (b_4 mode) are extension twins [44], while the operative {11$\bar{2}$2} twinning mode observed in Zr and Ti experiments (b_3 mode, as shown in Fig. 7b) are contraction twins. As a result, the b_3 {11$\bar{2}$2} contraction twins are profuse in *c*-axis compression of Ti and Zr, while the b_4 {11$\bar{2}$2} extension twins mostly form in *c*-axis tension of hcp materials. Under *c*-axis tension, the b_4 {11$\bar{2}$2} twins—formed by twin–twin interaction or through other mechanisms [30,32,34]—will directly compete with the primary {10$\bar{1}$2} twin in other regions of the same grain. Meanwhile, given the strong basal texture of rolled Mg and thus similar loading sense among many grains, these {11$\bar{2}$2} twins will also compete with the primary {10$\bar{1}$2} twins in other grains in the polycrystal aggregates. Therefore, the b_4 {11$\bar{2}$2} twin boundaries are not expected to show significant migration, given the high mobility of the primary {10$\bar{1}$2} twins. We emphasize that these immobile b_4 {11$\bar{2}$2} twins serve as strong barriers for subsequent slip and contribute to the unique strong strain hardening under *c*-axis tension.

4. Discussion

The orientation relation between the parent structure and variants T_2 and T_3 is directly extracted from our MD simulation as illustrated in Fig. 5e. Their orientation relation is consistent with that of the {11$\bar{2}$2} boundaries observed in our experiments of AZ31B (Figs. 1b and 2b). Specifically, the *c*-axis of the parent is also the common ⟨01$\bar{1}$0⟩-axis shared by variant T_2 and T_3. In other words, the misorientation between T_2 and T_3 is around 60° across the ⟨01$\bar{1}$0⟩ axis. Notably, this has an important implication that these twin boundaries, which form through twin–twin interactions, correspond to the aforementioned 55-60° ⟨01$\bar{1}$0⟩ peaks in the misorientation histograms obtained experimentally [16,24]. This relation is further supported by two facts. Firstly, this 60° ⟨01$\bar{1}$0⟩ peak is only prominent in the *c*-axis tension experiment, while absent from the *c*-axis contraction experiment [16]. This is because twin–twin boundary is only expected in the loading condition that permits extension twins—which is *c*-axis tension—because they are formed by the reaction of two extension twins. Secondly, Hong et al. [17] found that a peak emerged at 60°⟨01$\bar{1}$0⟩ when the strain reached 5%. Afterwards, this peak increased significantly, while, concomitantly, the peak at ~ 86°⟨$\bar{1}$2$\bar{1}$0⟩ kept decreasing. This is because the formation of twin–twin boundaries eliminates the original interacting extension twin boundaries.

Furthermore, twin–twin boundaries play an important role in strain hardening. Specifically, the {11$\bar{2}$2} boundary observed in our MD simulation does not migrate with subsequent loading. As pointed out by Roberts and Partridge [43], the two interacting {10$\bar{1}$2} twins have different shear directions and the resulting complex stress field blocks further growth of the two interacting twins. As a result, these immobile boundaries can significantly impede the dislocation motion in the same way as grain boundaries, leading to hardening for subsequent dislocation slip.

Finally, we note that the stress–strain curve of Mg shows a strong strain hardening unique to *c*-axis tension, while such hardening is absent from *c*-axis compression. The strain hardening behavior under *c*-axis tension is, in general, attributed to texture hardening and twin-boundary-induced dynamic Hall–Petch effect [40,41]. However, the predominant {10$\bar{1}$2} twin boundaries are extremely mobile—they can deposit easily into grain boundaries when the twin volume fraction is large, thus losing the hardening ability for subsequent slip. In contrast, the immobile {11$\bar{2}$2} twin–twin boundaries can serve as stronger barriers to dislocation motion. This is further substantiated by experimental observations that twin–twin boundaries provide sustained strain hardening in AZ31B alloy even after the volume fraction of {10$\bar{1}$2} twins starts to decrease [19].

5. Conclusions

In summary, we have combined EBSD analysis and atomistic simulations to study the {11$\bar{2}$2} twin–twin boundary in Mg. Experimentally, our EBSD analysis showed that many of the twin–twin boundaries align well with {11$\bar{2}$2} or {11$\bar{2}$6} planes. In addition, the evolution of boundary volume fraction and the strain hardening rate demonstrated that twin–twin boundaries contributed significantly to the sequential increase of the strain hardening rate in Stage II regime. Computationally, our MD simulations revealed dynamically the formation of {11$\bar{2}$2}

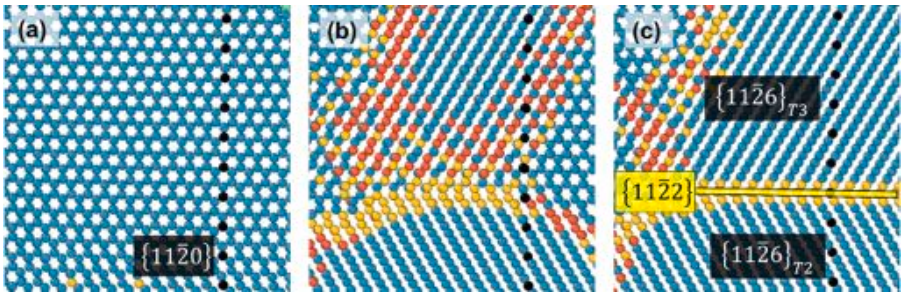

Fig. 6. The determination of K_2 plane for the equivalent twinning mode of the $\{11\bar{2}2\}$ twin–twin boundary. a) One $\{11\bar{2}0\}$ plane in the parent is traced in black. b) With the formation of two extension twins, the traced plane is found to transform into $\{11\bar{2}6\}$ planes in the two twin variants, T_2 and T_3. c) The formation of coherent $\{11\bar{2}2\}$ twin–twin boundary.

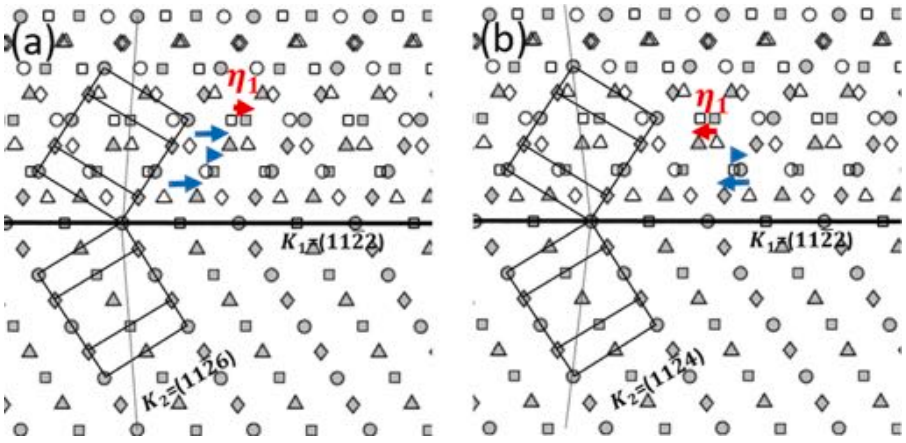

Fig. 7. Dichromatic complex of $\{11\bar{2}2\}$ twin boundary projected along $\langle 01\bar{1}0\rangle$ direction: (a) b_4 $\{11\bar{2}2\}$ extension twin and (b) b_3 $\{11\bar{2}2\}$ contraction twins. The twinning plane K_1 and shear direction η_1 and conjugate twinning plane K_2 are labeled in the figure. Bottom gray symbols and top open symbols represent the parent; top gray symbols represent the twin. The four symbols represent four adjacent $\{1\bar{1}00\}$ planes: circle is the plane of plane, diamond and square and triangle are $\sqrt{3}/2a$ and $\sqrt{3}/6a$ and $2/\sqrt{3}a$ below the paper respectively.

boundary via the interaction of two non-co-zone $\{10\bar{1}2\}$ twin variants. Moreover, to understand the relevance to recent studies on $\{11\bar{2}2\}$ twins in Mg and the $\{11\bar{2}2\}$ twins in Ti and Zr, the equivalent twinning mode of the $\{11\bar{2}2\}$ boundary were examined and the conjugate twinning plane was found to be $\{11\bar{2}6\}$. Finally, we point out that the $\{11\bar{2}2\}$ boundaries contribute significantly to the peak at 60° $\langle 01\bar{1}0\rangle$ in the misorientation histogram; moreover, they are critical to the unique strong strain hardening under c-axis tension of Mg and its alloys. The findings in this work is a critical step for completing the twinning theories for Mg and further applying twinning theories to better interpret experimental results.

CRediT authorship contribution statement

Amir Hassan Zahiri: Discussed the results, Writing of the manuscript. **Luiz Carneiro:** Discussed the results, Writing of the manuscript. **Jamie Ombogo:** Discussed the results, Writing of the manuscript. **Pranay Chakraborty:** Discussed the results, Writing of the manuscript. **Lei Cao:** Designed and directed the project, Discussed the results, Writing of the manuscript.

Declaration of competing interest

The authors declare that they have no known competing financial interests or personal relationships that could have appeared to influence the work reported in this paper.

Data availability

The data that support the findings of this study are available from the corresponding author upon reasonable request.

Acknowledgments

A. Zahiri, J. Ombogo, and L. Cao acknowledge the financial support from NSF-CMMI Mechanics of Materials and Structures Program, United States under Grant No. 1727428. L. Carneiro acknowledges the support from the U.S. National Science Foundation (CMMI-1762312). The authors would like to acknowledge the support of Research & Innovation and the Office of Information Technology at the University of Nevada, Reno, United States for computing time on the Pronghorn High-Performance Computing Cluster.

References

[1] M. Barnett, Twinning and its role in wrought magnesium alloys, in: Advances in Wrought Magnesium Alloys, Elsevier, 2012, pp. 105–143.
[2] T. Tang, S. Kim, M. Horstemeyer, Fatigue crack growth in magnesium single crystals under cyclic loading: Molecular dynamics simulation, Comput. Mater. Sci. 48 (2) (2010) 426–439, http://dx.doi.org/10.1016/j.commatsci.2010.02.003.
[3] S.N. Mathaudhu, E.A. Nyberg, Magnesium alloys in U.S. military applications: Past, current and future solutions, in: S.N. Mathaudhu, A.A. Luo, N.R. Neelameggham, E.A. Nyberg, W.H. Sillekens (Eds.), Essential Readings in Magnesium Technology, Springer International Publishing, Cham, 2016, pp. 71–76, http://dx.doi.org/10.1007/978-3-319-48099-2_10.
[4] I. Ostrovsky, Y. Henn, Present state and future of magnesium application in aerospace industry, in: International Conference "New Challenges in Aeronautics" ASTEC, vol. 7, 2007, pp. 19–22.
[5] J.A. Gann, Magnesium industry's lightest structural metal, SAE Trans. (1930) 620–641.
[6] D. Ando, J. Koike, Y. Sutou, Relationship between deformation twinning and surface step formation in AZ31 magnesium alloys, Acta Mater. 58 (13) (2010) 4316–4324.
[7] B. Li, E. Ma, Atomic shuffling dominated mechanism for deformation twinning in magnesium, Phys. Rev. Lett. 103 (3) (2009) 035503.

[8] I. Beyerlein, L. Capolungo, P. Marshall, R. McCabe, C. Tomé, Statistical analyses of deformation twinning in magnesium, Phil. Mag. 90 (16) (2010) 2161–2190.

[9] H. Fan, J.A. El-Awady, Molecular dynamics simulations of orientation effects during tension, compression, and bending deformations of magnesium nanocrystals, J. Appl. Mech. 82 (10) (2015) 101006.

[10] D. Brown, S. Agnew, M. Bourke, T. Holden, S. Vogel, C. Tomé, Internal strain and texture evolution during deformation twinning in magnesium, Mater. Sci. Eng. A 399 (1–2) (2005) 1–12.

[11] H. Fan, S. Aubry, A. Arsenlis, J.A. El-Awady, The role of twinning deformation on the hardening response of polycrystalline magnesium from discrete dislocation dynamics simulations, Acta Mater. 92 (2015) 126–139.

[12] J. Ombogo, A.H. Zahiri, T. Ma, L. Cao, Nucleation of $\{10\bar{1}2\}$ twins in magnesium through reversible martensitic phase transformation, Metals 10 (8) (2020) 1030.

[13] M. Barnett, Twinning and the ductility of magnesium alloys: Part I:"Tension" twins, Mater. Sci. Eng. A 464 (1–2) (2007) 1–7.

[14] M. Barnett, Z. Keshavarz, A. Beer, X. Ma, Non-Schmid Behaviour during secondary twinning in a polycrystalline magnesium alloy, Acta Mater. 56 (1) (2008) 5–15.

[15] R. Reed-Hill, E. Buchanan, Zig-zag twins in zirconium, Acta Met. 11 (1963).

[16] M.D. Nave, M.R. Barnett, Microstructures and textures of pure magnesium deformed in plane-strain compression, Scr. Mater. 51 (9) (2004) 881–885.

[17] S.-G. Hong, S.H. Park, C.S. Lee, Role of $\{10\bar{1}2\}$ twinning characteristics in the deformation behavior of a polycrystalline magnesium alloy, Acta Mater. 58 (18) (2010) 5873–5885.

[18] Q. Yu, J. Wang, Y. Jiang, R.J. McCabe, N. Li, C.N. Tomé, Twin–twin interactions in magnesium, Acta Mater. 77 (2014) 28–42.

[19] L. Carneiro, D. Culbertson, X. Zhu, Q. Yu, Y. Jiang, Twinning characteristics in rolled AZ31B magnesium alloy under three stress states, Mater. Charact. 175 (2021) 111050.

[20] L. Jiang, J.J. Jonas, A.A. Luo, A.K. Sachdev, S. Godet, Influence of $\{10\bar{1}2\}$ extension twinning on the flow behavior of AZ31 Mg alloy, Mater. Sci. Eng. A 445 (2007) 302–309.

[21] A. Oppedal, H. El Kadiri, C. Tomé, G. Kaschner, S.C. Vogel, J. Baird, M. Horstemeyer, Effect of dislocation transmutation on modeling hardening mechanisms by twinning in magnesium, Int. J. Plast. 30 (2012) 41–61.

[22] H. El Kadiri, J. Kapil, A. Oppedal, L. Hector Jr., S.R. Agnew, M. Cherkaoui, S. Vogel, The effect of twin–twin interactions on the nucleation and propagation of $\{10\bar{1}2\}$ twinning in magnesium, Acta Mater. 61 (10) (2013) 3549–3563.

[23] Q. Yu, J. Wang, Y. Jiang, R.J. McCabe, C.N. Tomé, Co-zone $\{10\bar{1}2\}$ twin interaction in magnesium single crystal, Mater. Res. Lett. 2 (2) (2014) 82–88.

[24] M. Lentz, R. Coelho, B. Camin, C. Fahrenson, N. Schaefer, S. Selve, T. Link, I. Beyerlein, W. Reimers, In-situ, ex-situ EBSD and (HR-) TEM analyses of primary, secondary and tertiary twin development in an Mg–4 wt% Li alloy, Mater. Sci. Eng. A 610 (2014) 54–64.

[25] N.E. Paton, W. Backofen, Plastic deformation of titanium at elevated temperatures, Metall. Trans. 1 (10) (1970) 2839–2847.

[26] M. Yoo, Slip, twinning, and fracture in hexagonal close-packed metals, Metall. Trans. A 12 (3) (1981) 409–418.

[27] J.W. Christian, S. Mahajan, Deformation twinning, Prog. Mater. Sci. 39 (1–2) (1995) 1–157.

[28] A.H. Zahiri, J. Ombogo, L. Cao, Formation of $\{11\bar{2}2\}$ contraction twins in titanium through reversible martensitic phase transformation, Scr. Mater. 195 (2021) 113694.

[29] A.H. Zahiri, J. Ombogo, T. Ma, P. Chakraborty, L. Cao, Transformation-induced plasticity in omega titanium, J. Appl. Phys. 129 (1) (2021) 015105, http://dx.doi.org/10.1063/5.0035465.

[30] A. Ostapovets, J. Buršík, K. Krahula, L. Král, A. Serra, On the relationship between $\{11\bar{2}2\}$ and $\{11\bar{2}6\}$ conjugate twins and double extension twins in rolled pure mg, Phil. Mag. 97 (14) (2017) 1088–1101.

[31] C. Cayron, R. Logé, Evidence of new twinning modes in magnesium questioning the shear paradigm, J. Appl. Crystallogr. 51 (3) (2018) 809–817.

[32] C. Cayron, A one-step mechanism for new twinning modes in magnesium and titanium alloys modelled by the obliquity correction of a (58, a+ 2b) prototype stretch twin, Acta Crystallogr. Sect. A: Found. Adv. 74 (1) (2018) 44–53.

[33] P. Chen, F. Wang, J. Ombogo, B. Li, Formation of $60\langle 01\bar{1}0\rangle$ boundaries between $\{10\bar{1}2\}$ twin variants in deformation of a magnesium alloy, Mater. Sci. Eng. A 739 (2019) 173–185.

[34] Y. Gao, J.-H. Ke, B. Mao, Y. Liao, Y. Zheng, L.K. Aagesen, Twinning path determined by broken symmetry: A revisit to deformation twinning in hexagonal close-packed titanium and zirconium, Phys. Rev. Mater. 4 (7) (2020) 070601.

[35] S. Plimpton, Fast parallel algorithms for short-range molecular dynamics, J. Comput. Phys. (1995) 1–19.

[36] S. Wilson, M. Mendelev, A unified relation for the solid-liquid interface free energy of pure FCC, BCC, and HCP metals, J. Chem. Phys. 144 (14) (2016) 144707.

[37] A. Stukowski, Visualization and analysis of atomistic simulation data with OVITO–the open visualization tool, Modelling Simulation Mater. Sci. Eng. 18 (1) (2009) 015012, http://dx.doi.org/10.1088/0965-0393/18/1/015012.

[38] D. Faken, H. Jónsson, Systematic analysis of local atomic structure combined with 3D computer graphics, Comput. Mater. Sci. 2 (2) (1994) 279–286.

[39] J.D. Honeycutt, H.C. Andersen, Molecular dynamics study of melting and freezing of small Lennard-Jones clusters, J. Phys. Chem. 91 (19) (1987) 4950–4963.

[40] N. Dixit, K.Y. Xie, K.J. Hemker, K. Ramesh, Microstructural evolution of pure magnesium under high strain rate loading, Acta Mater. 87 (2015) 56–67.

[41] A. Serra, D. Bacon, R. Pond, Twins as barriers to basal slip in hexagonal-close-packed metals, Metall. Mater. Trans. A 33 (13) (2002) 809–812.

[42] G. Agarwal, A.M. Dongare, Deformation twinning in polycrystalline Mg microstructures at high strain rates at the atomic scales, Sci. Rep. 9 (1) (2019) 1–11.

[43] E. Roberts, P. Partridge, The accommodation around $\{10\bar{1}2\}\langle 10\bar{1}1\rangle$ twins in magnesium, Acta Metall. 14 (4) (1966) 513–527.

[44] A. Serra, R. Pond, D. Bacon, Computer simulation of the structure and mobility of twinning disclocations in hcp metals, Acta Metallurgica Et Materialia 39 (7) (1991) 1469–1480.